




Circulating pulse cavity enhancement as a method for extreme momentum transfer atom interferometry

Rustin Nourshargh ^{1,2}, Samuel Lellouch^{1,2}, Sam Hedges ¹, Mehdi Langlois ¹, Kai Bongs¹ & Michael Holynski ¹✉

Large-scale atom interferometers promise unrivaled strain sensitivity to mid-band gravitational waves, and will probe a new parameter space in the search for ultra-light scalar dark matter. These proposals require gradiometry with kilometer-scale baselines, a momentum separation above $10^4\hbar k$ between interferometer arms, and optical transitions to long-lived clock states to reach the target sensitivities. Prohibitively high optical power and wavefront flatness requirements have thus far limited the maximum achievable momentum splitting. Here we propose a scheme for optical cavity enhanced atom interferometry, using circulating, spatially resolved pulses, and intracavity frequency modulation to meet these requirements. We present parameters for the realization of 20 kW circulating pulses in a 1 km interferometer enabling $10^4\hbar k$ splitting on the 698 nm clock transition in ^{87}Sr . This scheme addresses the presently insurmountable laser power requirements and is feasible in the context of a kilometer-scale atom interferometer facility.

¹School of Physics and Astronomy, University of Birmingham, Edgbaston B15 2TT, UK. ²These authors contributed equally: Rustin Nourshargh, Samuel Lellouch. ✉email: M.Holynski@bham.ac.uk

Atom interferometers are high-precision devices with a wide range of potential applications^{1,2}, from gravitational measurements^{3,4} to inertial sensing, navigation^{5,6}, and metrology^{7–9}. The measurement is inferred from the interference pattern between two coherent paths of an atomic wave function, which are split, reflected, and recombined through coherent pulses of light^{10,11}. Sensitivity is enhanced by increasing the space-time area of the interferometers¹² through large momentum transfer (LMT) techniques, and by increasing the total interrogation time. Recent proposals^{13–15} use atom interferometer gradiometry for gravitational wave^{16–21} and dark-matter^{22,23} detection, as they enable exploration of currently inaccessible frequency bands. These proposals require facility-scale sensors with kilometer-scale baselines and momentum separations of order $10^4\hbar k$.

Traditional atom interferometers rely on multiphoton interactions: two-photon Bragg²⁴ or Raman¹² transitions, or multiphoton Bragg^{25–27} transitions. Such techniques are sensitive to differential laser phase noise, making them challenging to implement in very large baseline systems where propagation delay causes the laser noise to dominate the overall noise budget. Differential single-photon interferometry benefits from greatly reduced susceptibility to laser noise and is the most promising technique for future large-scale interferometers^{28,29}. Large momentum transfer with sequential single-photon transitions has been demonstrated in ^{88}Sr ³⁰, achieving interferometry with a momentum separation of $141\hbar k$ ³¹. Extending the technique to $10^4\hbar k$ raises significant challenges. Spontaneous emission must be minimized during the interferometry sequence, motivating the use of transitions to long-lived excited states, such as those used in atomic clocks^{32,33}. The weak coupling to these long-lived excited states requires high optical powers to match the Rabi frequencies that can be achieved on short-lived states.

The 698 nm optical clock transition in ^{87}Sr is a suitable candidate for single-photon interferometry. With an excited state lifetime of 118 s ($\Gamma = 2\pi \cdot 1.35$ mHz), spontaneous emission is a negligible source of decoherence³⁴. In order to complete the $10^4\hbar k$ pulse sequence in a small fraction of the second-scale total interrogation time, π -pulse durations in the 1–10 μs range are needed. The Rabi frequency for this transition is given by $\Omega = \Gamma\sqrt{I/2I_s}$, with saturation intensity $I_s = 0.4$ pW cm^{-2} , resulting in an optical intensity requirement ≈ 5 kW cm^{-2} . Geometric constraints arising from free-space propagation over a 1 km baseline result in a minimal input beam radius of 15 mm and a prohibitively large optical power of ≈ 20 kW. Delivering these pulses with a uniform phase also demands flat optical wavefronts³⁵. These constraints have prevented momentum separations of $10^4\hbar k$ from being achieved thus far.

Optical cavities offer a potential solution to both of these problems³⁶: resonant power enhancement reduces the required input power, and spatial filtering improves wavefront flatness. Impressive early demonstrations of cavity-enhanced interferometry have shown the potential of these systems^{37,38}. However, cavity power enhancement is only effective if the pulse duration exceeds the cavity lifetime. For pulses shorter than, or comparable to the cavity lifetime the cavity fails to reach its maximum power enhancement. The intracavity field persists long after the input light is removed resulting in significant pulse elongation. This bandwidth limit, described by Alvarez et al.³⁹, restricts the maximum length-finesse product that can be achieved without significant pulse elongation. In a kilometer-scale cavity, the bandwidth limit restricts the maximum finesse to $\mathcal{F} \leq 10$, significantly reducing the mode filtering and power enhancement benefits.

We present a scheme based on circulating, spatially resolved pulses to overcome the bandwidth limit and satisfy the challenging pulse requirements for $10^4\hbar k$ LMT. A circulating pulse

drives a π -pulse once per round trip, removing the need to couple a new pulse into the cavity for each beam splitter. This avoids lifetime elongation and overcomes the bandwidth limit, dramatically increasing the possible cavity lengths and finesse that can be exploited. We present parameters for a cavity and laser system capable of $10^4\hbar k$ momentum separation on the 698 nm transition in ^{87}Sr . Such LMT is commensurate with the sensitivity requirements for future dark-matter and gravitational-wave detectors, as described in¹⁵.

Results

Consider a traveling wave cavity into which we periodically couple short, spatially resolved pulses of light. We present an example cavity with 1 km baseline and round trip path length of 6 km (see Fig. 1). This scale is relevant in the context of recent proposals^{13,15} but in principle, the scheme is applicable to any traveling wave cavity. To align with recent proposals^{13,15}, we assume here that the cavity has a 1 km baseline and a round trip path length of 6 km (see Fig. 1). We use a pulse duration $\tau = 6$ μs , which corresponds to a length of 1.8 km and satisfies the condition for spatially resolved pulses; see Methods. Successive pulses coupled into a single circulating mode are separated by the cavity round-trip time (20 μs) such that they constructively interfere. This periodic train of pulses forms a comb in the frequency domain, but in this regard, it is identical to free-space LMT schemes using periodic short pulses. Light is coupled in away from atomic resonance, and shifted onto resonance using Serrodyne modulation once a stationary regime has been reached (see Fig. 2), resulting in a high-intensity pulse circulating inside the cavity. The circulating pulse intensity is adjusted to drive a π -pulse on the atoms loaded in the cavity, delivering a momentum kick of $\hbar k$ on each round trip. To ensure successive momentum contributions add constructively, we alternate the pulse direction by populating both circulating modes of the cavity. After 100 ms, 5000 round trips have taken place and the target splitting of $10^4\hbar k$ is achieved.

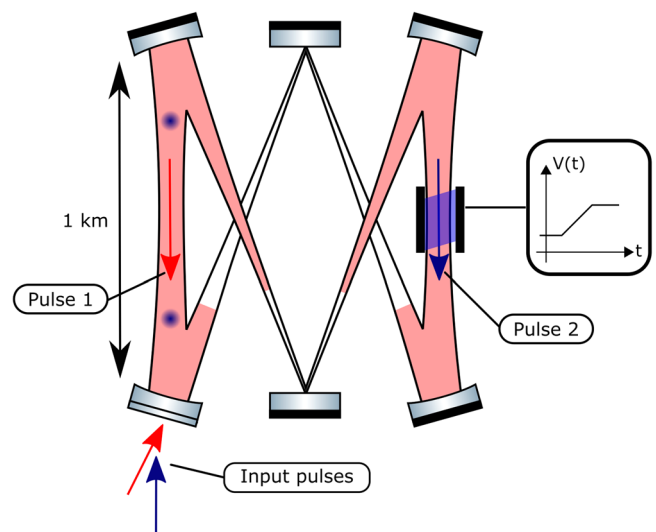


Fig. 1 Circulating pulse interferometry schematic. Circulating pulses occupy each of the two running wave modes in this example cavity, 6 km round trip with a 1 km baseline aligned with gravity. On each round trip, additional light is coupled into the cavity to compensate for losses. Serrodyne modulation, applied through a Pockels cell, shifts the frequency of each pulse on each pass to compensate for Doppler shifts. The pulse durations are maximized within the constraint that only one pulse may pass through the atoms (blue) or Pockels cell at a time.

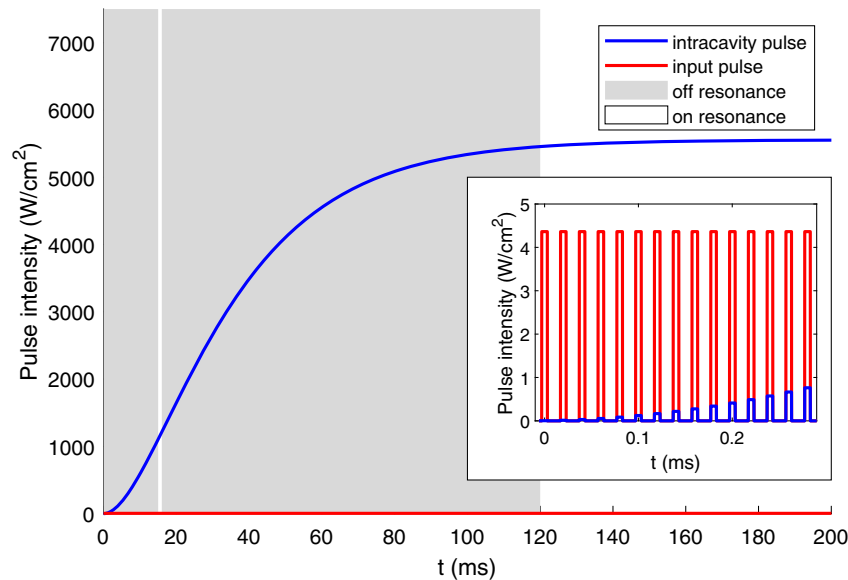


Fig. 2 Cavity build up. Cavity response to a periodic train of spatially resolved coherent square pulses as a function of time. The input intensity I_{in} is plotted in red and the intracavity intensity I_{circ} in blue. The main plot shows the intensity maxima of the input and circulating pulses. The inset shows the full time-dependence for the first 15 input pulses. The system parameters match those described in the text, $L = 6$ km, $\mathcal{F} = 4000$, $\tau = 6 \mu\text{s}$. The intracavity intensity increases as input pulses coherently add, before saturating at its stationary cavity-enhanced value, which is exactly that of a π -pulse. Grey-shaded areas indicate when the light is off-resonance with the atomic transition. It is shifted on-resonance for one round trip at $t = 15$ ms to drive the initial $\pi/2$ -pulse, and again after 120 ms to perform the large momentum transfer sequence.

In this beam splitter sequence, momentum is only imparted to one arm of the interferometer (referred to as the *fast-arm*), leaving the other (*slow-arm*) unaffected. Lifting the initial degeneracy between arms requires careful treatment, outlined in Methods.

Cavity build-up and pulse requirements. In the following analysis, we consider only one of the two running wave modes of the cavity containing the circulating pulses, but note that the results apply equally to both. The input intensity is fixed by the requirement that the circulating pulse drives a π -transition on the atoms. The response of the intracavity field to the train of phase-coherent input pulses is obtained by solving the propagation equation where t is the transmission coefficient of the input mirror, $(1 - \gamma)$ is the total round trip loss, τ_{rt} is the round-trip duration, and $i = \sqrt{-1}$. If we select $t = \gamma/\sqrt{2}$ such that the cavity is impedance matched, this is given by:

$$E_{circ}(t) = itE_{in}(t) + \gamma E_{circ}(t - \tau_{rt}) \quad (1)$$

The circulating pulse amplitude increases with each successive input pulse before reaching a stationary value where further pulses only compensate for round-trip losses; see Fig. 2. The stationary pulse intensity is cavity enhanced $I_{circ}(t) = (\mathcal{F}/\pi)I_{in}(t)$ where \mathcal{F} is the finesse⁴⁰. Cavity enhancement allows this scheme to achieve π -pulses inside the cavity with reduced input laser power. A finesse of 4000 enables $6 \mu\text{s} \pi$ -pulses with an input intensity, at the center of the beam, of only 4.4 W cm^{-2} , compared to 5.6 kW cm^{-2} without cavity enhancement. This represents a 1000-fold reduction in required laser power, putting it within reach of existing laser technology; see Methods.

The total power required depends on the radius of the laser beams, with lower bounds of both atomic and optical origin. High-fidelity pulses can only be achieved if the intensity profile does not vary across the atomic cloud. A beam to cloud diameter ratio of 20 ensures the impact of residual intensity variations on fidelity loss is less than 0.1%. For a typical cloud radius of $200 \mu\text{m}$, a $1/e^2$ beam radius of 4 mm is sufficient, requiring a total input

power of 1.1 W ^{41,42}. However, divergence of the Gaussian beam over the 1 km arm length is a more stringent constraint. The minimum beam radius at 500 m from the waist, $w = 15$ mm, is produced with a beam waist $w_0 = 10.5$ mm. With the circulating intensity, mode radius, and power enhancement previously defined, the minimum required input laser power is 16 W. Since the beam radius, and therefore intensity, varies with position along the optic axis, longer atomic freefall times may necessitate increased beam diameters to achieve required axial intensity homogeneity.

The required input optical power decreases linearly with finesse and quadratically with pulse duration. The need to avoid pulse overlap at the atoms constrains the maximum pulse duration; see Methods. Figure 3 shows the minimum optical input power required as a function of round-trip path length, for cavities with a baseline of 1 km and differing values of finesse. The clear reduction in input power motivates the use of large high-finesse cavities. The increase in the time taken to reach the stationary regime (linear in both length and finesse) is not a limiting factor in the proposed scheme.

Interferometer sequence. Pulses of light are coupled into the cavity far-detuned from atomic resonance, avoiding unintentional interactions during the build-up phase. Once the target amplitude has been reached (white areas in Fig. 2), intracavity serrodyne modulation is used to shift the circulating pulse onto atomic resonance. Serrodyne modulation is generated by applying a linear ramp to an intracavity Pockels cell. High modulation efficiencies and low losses are essential to reaching the required pulse amplitude; some experimental steps toward realizing this are discussed in the Methods.

At $t = 15$ ms the circulating amplitude has reached that of a $\pi/2$ -pulse and one of the pulses is shifted onto resonance for a single round trip, see white vertical line on Fig. 2. This delivers a $\pi/2$ -pulse and is followed by a further serrodyne shift to move the pulse away from resonance whilst the amplitude is increased further.

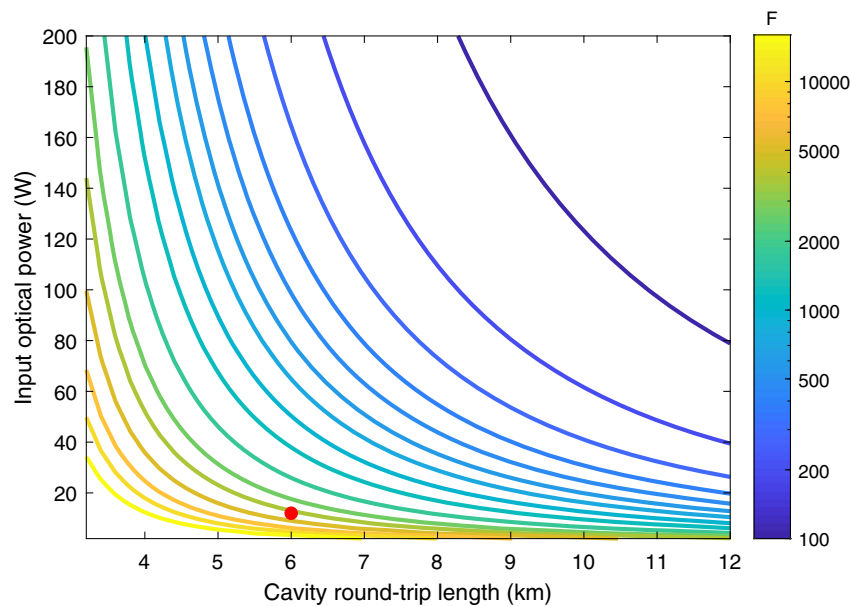


Fig. 3 Input power requirements. Required input optical power as a function of cavity round-trip length and finesse \mathcal{F} . The cavity baseline is fixed at 1 km, and the maximum pulse duration, minimizing power requirements, is selected. This is the limiting value for the pulses to avoid spatial overlap at the atoms; see Methods. The parameters used throughout are indicated by the red dot.

We propose two techniques to lift the initial arm degeneracy: imparting momentum to the slow-arm of the interferometer with the 689 nm transition, and bichromatic beam splitter pulses to track the recoil of both arms.

At $t = 120$ ms, the circulating intensity has reached the value required for a π -pulse and the initial degeneracy has been lifted. Intracavity serrodyne modulation is used to shift both circulating pulses onto resonance with the fast-arm of the interferometer. On each round trip they deliver a pair of sequential counter-propagating π -pulses, imparting $2\hbar k$ of momentum. Recoil shifts and gravitationally induced Doppler shifts are compensated every round trip with further serrodyne modulation. After 5×10^3 round trips, a momentum separation of $10^4 \hbar k$ between the interferometer arms has been achieved. The circulating pulses are either dumped from the cavity or serrodyne shifted back away from resonance in preparation for the next beam splitter. Similarly constructed beam splitter sequences are used to recombine and close the interferometer. The total interferometer sequence duration is less than 1 s, a duration over which spontaneous emission losses remain negligible.

Doppler shift and phase compensation. In addition to its primary role of shifting pulses on and off the atomic resonance, serrodyne modulation is used to compensate for Doppler shifts in the sequence. Figure 4 shows the fast-arm recoiling upwards on each successive beam splitter pulse. The Doppler effect will cause the downward-going pulse to appear blueshifted, whilst the upward-going pulse appears redshifted. We compensate for this by applying negative serrodyne shifts to the downward-going pulse and positive shifts to the upward-going pulse. The shifts must be applied to the two pulses separately, requiring them to pass through the Pockels cell at different times.

Serrodyne modulation changes the phase relationship between the circulating and input light. To ensure constructive interference continues, it is vital that the circulating and input pulses remain in phase. Phase compensation can be achieved through active control of the input light or additional voltages on the Pockels cell; see Methods.

Large momentum transfer fidelity. Reaching a momentum transfer of $10^4 \hbar k$ requires 10^4 beamsplitter pulses, which must be of high-fidelity to maintain contrast through the interferometer. There are several factors limiting the fidelity of an atom-optic pulse: the thermal velocity spread of the cloud (which results in a dispersion in the Doppler shifts), the spatial variations of the beam intensity at the scale of the cloud, and the spontaneous emission losses. These constraints apply to any scheme requiring high-fidelity LMT with or without cavity enhancement. Using the parameters presented thus far, we find that we can maintain sequence fidelity at $10^4 \hbar k$. The fidelity improves with increased beam-to-cloud diameter ratio, with a strong dependence up to a ratio of 20. At this ratio, the intensity is approximately constant at the scale of the cloud and further increasing the beam diameter results in only a minor improvement in fidelity. The fidelity also improves for reduced atom cloud temperature, and in our scheme temperature is the limiting parameter. This arises from the Doppler shift dispersion inside the cloud, and not from the spatial expansion of the cloud during its propagation, which remains negligible. For a cloud radius of 200 μm (beam-to-cloud ratio of 75), the sequence fidelity is plotted for various cloud temperatures, see Fig. 5. We observe that to achieve sufficient contrast at the output of the interferometer, a temperature of a few nanokelvin is required for $10^4 \hbar k$ LMT⁴³. This is aligned with the objectives stated in ref. 15 for dark-matter and gravitational-wave detectors (see especially sensitivity plots therein for a comparison between the existing and future facilities performance).

Discussion

We have presented a scheme for cavity-enhanced atom interferometry to enable extremely large momentum transfer beam splitters in large-scale atom interferometers. Intracavity serrodyne modulation allows circulating, spatially resolved pulses to be recycled, overcoming cavity lifetime elongation and the pulse bandwidth limit. Serrodyne modulation is used to shift the pulse on and off-resonance, and compensate for photon recoils and gravitational Doppler shifts.

We analyze the case of a kilometer-scale atom interferometer for gravitational wave detection, and find that a cavity with 6 km

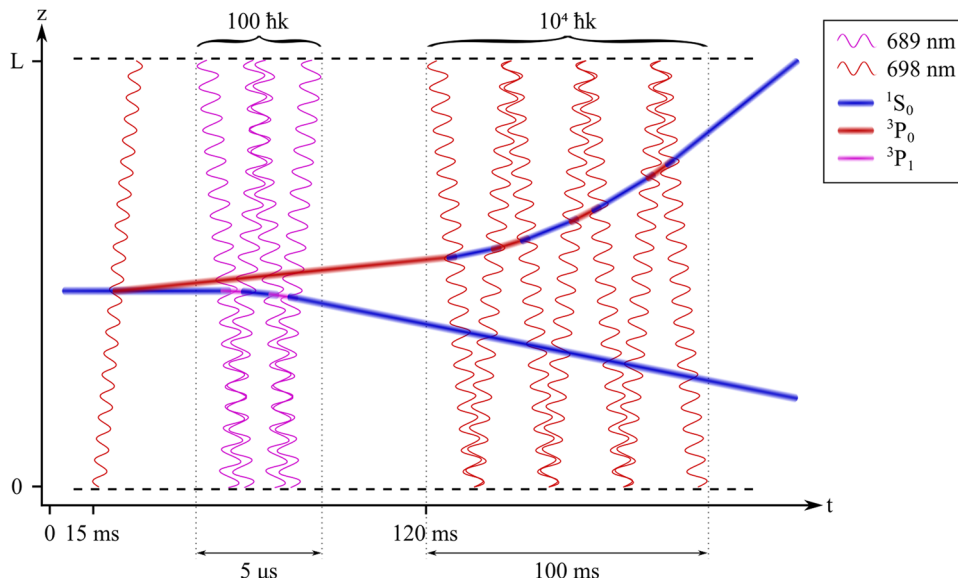


Fig. 4 Space-time diagram for large momentum transfer atom interferometry. An initial 698 nm (red, wavy) $\pi/2$ -pulse transfers the atoms into a superposition between the ground state, slow-arm (blue), and the excited state, fast-arm (red). Sequential counterpropagating π -pulses on the 689 nm transition (pink, wavy) deliver $100\hbar k$ of momentum to the slow-arm only. With the frequency degeneracy lifted, the main large momentum transfer sequence begins at 120 ms, delivering $10^4\hbar k$ of momentum to the fast-arm through counterpropagating π -pulses on the 698 nm transition.

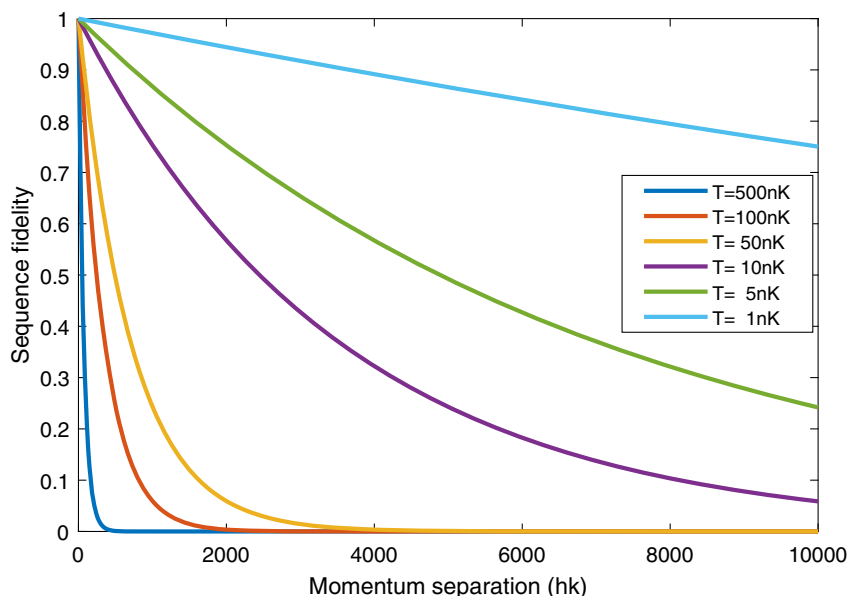


Fig. 5 Pulse sequence fidelity. Fidelity of the entire LMT (large momentum transfer) sequence as a function of momentum separation, for various atomic temperatures. The sequence fidelity is obtained as the cumulative product of individual pulse fidelities, which are obtained by averaging the transition probability over the cloud instantaneous spatial and velocity distributions. The initial cloud radius is $200\ \mu\text{m}$ and the beam radius is 1.5 cm. To obtain a sufficient contrast at the end of the $10^4\hbar k$ LMT sequence, a cloud temperature less than 10 nK is required. Cloud expansion, Doppler shift compensation and spontaneous emission are included in the model. The pulse bandwidth is neglected, but any resulting errors can be compensated with frequency and intensity adjustments^{55,56}.

round trip path length and a finesse of $\mathcal{F} = 4000$ generates a circulating pulse intensity of $5.6\ \text{kW cm}^{-2}$ with only $4.4\ \text{W cm}^{-2}$ at the input. When applied to the ^{87}Sr 698 nm clock transition this enables $6\ \mu\text{s}\pi$ -pulses in a mode of 1.5 cm radius with an input laser power of only 16 W. The overall sequence fidelity is found to be limited by the temperature of the atomic cloud. A beam splitter with $10^4\hbar k$ momentum separation between the arms and combined fidelity > 0.25 requires a vertical velocity spread of

1.2 mm/s, corresponding to a temperature selectivity of 5 nK. Further reductions in cloud temperature increase fidelity and hence the maximum total momentum separation. This is the first practical, albeit challenging, approach to the generation of short, high-fidelity pulses on such optical transitions. Practical implementation of the scheme at scale, and addressing several of the challenges, would require a long term development programme and facility approach.

However, circulating pulse interferometry could also be tested on a 10 m atom interferometer operating on the 689 nm $^1S_0 - ^3P_1$ transition in ^{87}Sr . The higher Rabi frequency enables shorter pulses and a correspondingly smaller cavity. Whilst spontaneous emission will limit the performance on this transition below the target of $10^4 \hbar k$ momentum separation, this will still provide a useful performance enhancement to these lab-scale systems, and serve to validate the scheme.

Furthermore, a more detailed treatment is required to fully assess the scheme and systematic effects that are introduced or mitigated. An example is effects due to the light field accumulated during the cavity build-up time, which gives rise to light shifts and an effective radial trapping. For instance, with the parameters used in the example case here, this gives rise to a 328 kHz shift for the ground state, before taking into account reductions due to the circulating nature of the pulse. Such shifts can be mitigated through use of gradiometry, yet a residual difference of 6.5 kHz light shift remains due to the cavity geometry and the positioning and length of each interferometer, with this being relevant both between interferometers and interferometer arms. This could be mitigated through the design of the cavity geometry and circulating pulse parameters, as well as the choice of atom and atom interferometry scheme and baseline. Such aspects are under investigation in a follow-on study.

By overcoming the bandwidth limit we have enabled optical cavity enhancement of the largest proposed atom interferometers. Circulating pulse cavity-enhanced atom interferometry offers a step change in large momentum transfer atom interferometry. With a 1000-fold increase in optical intensity, it enables large-scale atom interferometers for gravitational wave detection and new tests of fundamental physics.

Methods

Initial arm degeneracy. Our scheme relies on velocity selective pulses such that only one arm of the interferometer is addressed, leaving the other unaffected. However, the large Rabi frequency (≈ 80 kHz) and small initial frequency separation from the first $\pi/2$ -pulse (9.4 kHz) results in the two arms being initially degenerate. The two arms cannot be discriminated in frequency with high-fidelity until the frequency separation exceeds the pulse bandwidth. Since one recoil of $\hbar k$ produces a Doppler shift of $\hbar k^2/m = 2\pi \cdot 9.4$ kHz, $\approx 10 - 100$ beam splitters are required to lift this degeneracy.

One method to open the interferometer is to create the initial momentum separation with π -pulses on the $^1S_0 - ^3P_1$ 689 nm transition. The initial $\pi/2$ -pulse on 698 nm splits the atoms into a superposition of the long-lived excited state and the ground state, referred to as the fast and slow-arm respectively. We apply one hundred sequentially counterpropagating π -pulses on the 689 nm transition, imparting $100\hbar k$ of momentum to the slow-arm on the interferometer whilst leaving the fast-arm in the excited state unaffected. The resulting Doppler shift is $100\hbar k^2/m \approx 2\pi \cdot 1$ MHz, greatly exceeding the Rabi frequency of the clock pulses, ensuring that the fast-arm of the interferometer can be uniquely addressed.

The 689 nm transition allows for much higher Rabi frequencies ~ 100 MHz, enabling 10 ns π -pulses without cavity enhancement. The 100 pulse sequence is completed within 5.3 μs : 3.3 μs for the pulses to propagate 1 km between the clouds and ≈ 2 μs for 100 pulses. The pulse bandwidth is large compared to the total Doppler shift so we achieve high-fidelity beam splitters without Doppler compensation³¹. The 3P_1 state has a lifetime of 21.6 μs requiring a rapid pulse sequence ending in the ground state to minimise losses due to spontaneous emission. This beam splitter sequence can be accommodated within the general scheme depicted on Fig. 2 and performed during the cavity build-up time, when the 698 nm pulses are far-detuned from atomic resonance. This sequence must be implemented without cavity enhancement to avoid residual 689 nm light driving parasitic transitions from the interferometer. Two lasers located at either end of the interferometry region drive the pulse sequence whilst minimising the duration spent in the relatively short-lived $5s5^3P_1$ state. This requires cavity mirrors be highly transmissive at 689 nm while being highly reflective at 698 nm; this could be implemented with orthogonal polarizations for the two wavelengths.

An alternative approach circumvents the issue of arm degeneracy, using only the 698 nm clock transition, by utilizing two polarization modes in each pulse. These polarization modes are oriented orthogonally and co-planar with the plane of the cavity, such that these polarisations are maintained following reflection. The two polarization modes are independently serrodyne shifted to track the Doppler shifts experienced in both arms of the interferometer, redshifting one polarization whilst blueshifting the other. As both interferometer arms are now recoiling, the total number of beam splitter pulses required to achieve a given momentum separation is halved. This scheme requires two Pockels cells to apply a phase shift to one of the two polarizations whilst leaving the other unchanged. Cells based on $42m$ class crystals have this property if the r_{63} coefficient is employed in a transverse configuration⁴⁴. This geometry results in a residual birefringence from each crystal, which we compensate by arranging the two crystals orthogonally. Phase compensation can be achieved with the same methods discussed in the results, but must now be applied to both polarizations simultaneously.

This dual-polarization, dual-frequency scheme requires careful control of the light intensities on a pulse-by-pulse basis to ensure this bichromatic light field delivers high-fidelity π -pulses to both arms on each round trip. The details of the specific powers and frequencies required to achieve this are beyond the scope of this paper.

Maximum pulse duration. The scaling of input power with pulse duration motivates the use of the longest pulses possible. However, the interferometry scheme described in this work requires successive pulses to alternate in direction and to be temporally distinct when they pass through the atoms and the Pockels cell. This constrains the maximum pulse duration.

We define an exclusive length L_{ex} as the region within the cavity where the pulses must not overlap. Two pulses, of equal limiting duration τ_{max} , propagating in opposite directions, will fully overlap when one pulse leaves the exclusive length and the other is about to enter. This condition is repeated on both sides of the exclusive length. Symmetry considerations show that there is an equal exclusive length on the opposite side of the cavity. Figure 6 illustrates the locations of the pulses and exclusive length in a generalized ring cavity. Summing the exclusive length and pulse length the condition becomes clear:

$$\tau_{\text{max}} = \frac{1}{2c} (L_{\text{RT}} - 2L_{\text{ex}}) \quad (2)$$

For pulses with $\tau \leq \tau_{\text{max}}$ and correct input timings, singular occupation of the exclusive lengths will be achieved. Pulse durations approaching τ_{max} reduce performance requirements for the cavity and input lasers. The cavity presented in this paper has $L_{\text{RT}} = 6$ km and $L_{\text{ex}} = 1$ km yielding $\tau_{\text{max}} = 6.66$ μs , just exceeding the selected pulse duration of $\tau = 6$ μs .

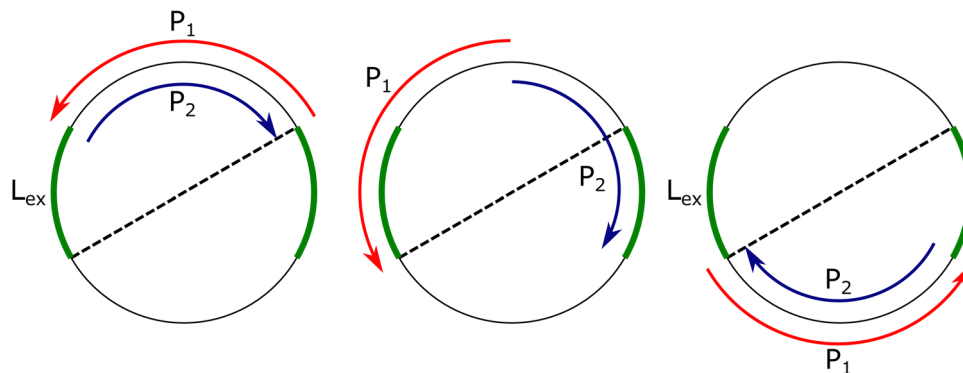


Fig. 6 Circulating pulse duration limits. This figure shows two counterpropagating pulses of maximal duration τ_{max} circulating in a cavity with round trip path length L_{RT} represented by the circumference of the circle. In the first frame pulse-2 has just left the exclusive length (L_{ex}) and pulse-1 is about to enter it. The condition for singular occupation of the exclusive length is clear from the first and third frames $L_{\text{RT}}/2 = L_{\text{ex}} + c \tau_{\text{max}}$ where c is the speed of light.

Control of frequency and phase. Frequency and phase shifts arise during the sequence that require active control. There are two sources of frequency shift both caused by the Doppler effect: photon recoil and gravitational acceleration. Recoil shifts are caused by the absorption or emission of a photon, and affect the fast-arm of the interferometer during the main LMT sequence. Each recoil event causes a change in the velocity of the atoms, leading to a Doppler shift of $\hbar k^2/m = 2\pi \cdot 9.4$ kHz per recoil. Gravity accelerates both arms of the interferometer downwards and causes an additional Doppler shift of 14 MHz/s, or 281 Hz per round trip. We track these shifts by applying serrodyne modulation to each of the two circulating pulses. When a pulse travels through the Pockels cell a serrodyne shift is applied. High-efficiency modulation is achieved by applying a single, linear ramp for the duration of the pulse⁴⁵. This avoids the bandwidth limitations encountered with sawtooth waveforms. This is a $\chi^{(2)}$ effect, so the phase shift ϕ , is proportional to applied voltage:

$$\phi = \pi \frac{V(t)}{V_\pi} = \pi \frac{V_0 + kt}{V_\pi} = \phi_0 + \frac{\pi kt}{V_\pi} \quad (3)$$

Frequency is defined as $d\phi/dt$ so a linear phase chirp produces a frequency shift. By adjusting the value of k the frequency can be shifted by up to $1/\tau$ Hz for a standard length Pockels cell, (ramping from $\phi = -\pi \rightarrow \pi$ over the pulse duration τ). For $\tau = 6 \mu\text{s}$ this gives a single pass frequency shift of up to 160 kHz, which is significantly larger than the 9.4 kHz frequency shifts induced by recoil and gravitational Doppler shifts every round trip. This voltage range and repetition rate are comparable to those encountered in q-switched lasers, and the required voltage ramp rate is orders of magnitude slower⁴⁶. If larger shifts are needed for the initial frequency steps on and off-resonance the modulation bandwidth can be increased up to N/τ Hz with an extended length $N\pi$ -Pockels cell without increasing the voltage requirements. The performance of this scheme is limited by the modulation efficiency and any losses associated with the modulator itself. Both circulating modes use the same polarization of light, so reflection losses can be reduced by using a Pockels cell with Brewster's angle cut crystal facets⁴⁷.

Phase compensation can be achieved in two ways. DC voltages can be applied to the intracavity Pockels cell to ensure that the phase on the input mirrors is constant for every pulse in both circulating modes. The voltages required will differ every round trip, and be different for each circulating mode. Longer Pockels cells will increase flexibility to introduce a phase shift whilst leaving enough headroom for modulation. A simpler approach experimentally, is to adjust the phase of the input pulses on each round trip to match that of the circulating field. A Pockels cell or acousto-optic modulator on each of the input beams could achieve this in an agile and controllable way. Regardless of which phase compensation technique is adopted, the frequency of the input beams must also be tuned to track the circulating fields.

Cavity Stabilisation. Unlike cavities in which light fully occupies the mode, the circulating pulse scheme does not require the length of the cavity to be stabilised to a small fraction of a wavelength. Instead the input pulse must simply be in phase with the circulating pulse. A high bandwidth feedback loop stabilises the input light to the circulating pulse on a pulse by pulse basis⁴⁸. The phase of the circulating pulse can be measured in advance of the input pulse coupling by sampling a small amount of light through a second mirrors 2 km of travel time in advance of the main input. This allows additional time for the input phase to be adjusted reducing bandwidth requirements on the feedback loop. High passive stability of the cavity or an independent cavity length stabilisation system, using a second wavelength CW, would both simplify the agile phase control stabilisation requirements. The phase stabilisation system for this scheme is a unique technical challenge and will require detailed study in the construction of this instrument.

Optical damage. The optical intensity required in our scheme is 5.6 kW cm^{-2} at near continuous wave duty cycle. This is within the damage thresholds measured in a BBO Pockels cell (beta barium borate) at 1064 nm over 20 years ago⁴⁹. Whilst this is not directly applicable to performance at 698 nm it suggests that these intensity levels are feasible.

Frequency shifting. Pockels cells are commonly used for q-switch applications with 1 ns switching times commonly reported. In very large crystals this may increase to 10 ns. The linear ramp proposed for serrodyne modulation spans the same voltage range as a q-switch in 6 μs . Generating a linear high voltage ramp on this timescale remains challenging but compared to the rise time requirements in a q-switch is feasible.

Crystal aperture. A large crystal diameter is required to accommodate the mode without introducing significant aperture losses. Normalised power transmission through a circular aperture is given by $1 - \exp(-2a^2/w^2)$ where a is the radius of the aperture and w is the Gaussian beam radius⁴⁰. Transmission losses below 10^{-4} require $a > 2.15w$, which for our system parameters require a Pockels cell diameter of 64 mm. This is a large Pockels cell but cells of this size are commercially available. A secondary issue arising from finite input aperture is diffraction which will cause wavefront aberrations, again constraining the minimum Pockels cell

aperture size. These diffraction effects should be evaluated for the aperture shape under consideration, including any possible mitigating actions such as apodization.

Loss. Pockels cells are available commercially with a single pass insertion loss below 1.5%. Some of this loss is caused by windows for hermetic sealing which in a vacuum chamber are unnecessary. Without considering possible improvements, an impedance matched round trip cavity loss of 3% limits the finesse to 200 and the power enhancement to 70 times. This still represents a significant increase in available optical power compared to the free-space case. Whilst this enhancement is a factor of 20 smaller than the parameters described in the main text, by increasing the input power to 320 W, interferometry performance can be maintained. Whilst this is a significant laser power it is within an order of magnitude of high power lasers already used in atom interferometry⁵⁰ and 60 times less than the 20 kW required without cavity enhancement. Thermal dissipation in the crystal will be significant even for a highly transmissive crystal, and the management of the thermal loads of the crystal requires further investigation. A full-scale experiment will be a facility-scale undertaking, justifying developments in both Pockels cells and lasers to meet the performance requirements.

Cavity geometry. Mirror curvatures or a detailed cavity geometry are not presented here, as a fully optimised geometry will need to model the optimum mode radius at the centre of the Pockels cell considering clear aperture, loss, and damage threshold alongside analysis of round trip Gouy phase to optimise the spatial mode spectrum^{40,51}. An infinite number of solutions exist by varying the curvatures of each pair of mirrors and spacing between these. By way of example consider a highly symmetric case where the mode radii at the centres of interferometry and Pockels cell arms are equal. This can be implemented with four identical curved mirrors in the four corners and two planar mirrors in between these. By varying the radii of curvature of these four mirrors between 2 km and 5 km the round trip Gouy phase can be tuned over the full range, allowing optimised higher-order spatial mode control. Tuning mirror curvature in this way also changes the mode radii but adjusting mirror pairs independently allows this to be prevented.

Laser system. This scheme places demanding constraints on the input lasers, requiring narrow linewidth, rapid tunability, and high output power. It will require at least two separate lasers to inject light into both circulating modes of the cavity. The coherence length of the lasers must exceed the average distance traveled by a photon within the cavity. This ensures that successive input pulses continue to constructively interfere with the intracavity circulating pulse. With a cavity photon lifetime of $t_c = L\mathcal{F}/\pi c \simeq 30$ ms, a laser linewidth of ~ 1 Hz will ensure the limit is comfortably met. The optical paths on the input to the cavity must also be phase stable at ~ 1 Hz level. These performance levels are demanding, but regularly achieved in optical clock lasers operating on the 698 nm transition^{52,53}.

Clock lasers do not typically produce the output powers required for this scheme, so we propose the use of a clock laser as the master to injection-lock a high power slave⁵⁴. Commercially available high power Ti:sapphire lasers generate ≥ 5 W, so the required output of 16 W would require the coherent combination of four of these. The pulsed nature of the output may allow the use of a single Q-switched slave laser, reducing the system complexity. Injection locking also simplifies frequency and phase compensation which may be accomplished by appropriate modulation of the master laser, prior to injection seeding. This retains the stability properties of the master laser and allows modulation to occur at low power levels.

Data availability

The authors declare that all data supporting the findings of this study are available within this article and Supplementary Material. It can be available from the corresponding author upon reasonable request.

Code availability

The code that supports the findings of this study can be available from the corresponding author upon reasonable request.

Received: 14 April 2021; Accepted: 22 September 2021;

Published online: 02 December 2021

References

1. Cronin, A. D., Schmiedmayer, J. & Pritchard, D. E. Optics and interferometry with atoms and molecules. *Rev. Mod. Phys.* **81**, 1051–1129 (2009).
2. McGuirk, J. M., Foster, G. T., Fixler, J. B., Snadden, M. J. & Kasevich, M. A. Sensitive absolute-gravity gradiometry using atom interferometry. *Phys. Rev. A* **65**, 033608 (2002).

3. Rosi, G., Sorrentino, F., Cacciapuoti, L., Prevedelli, M. & Tino, G. M. Precision measurement of the Newtonian gravitational constant using cold atoms. *Nature* **510**, 518–521 (2014).
4. Fixler, J. B., Foster, G. T., McGuirk, J. M. & Kasevich, M. A. Atom interferometer measurement of the Newtonian constant of gravity. *Science* **315**, 74–77 (2007).
5. Durfee, D. S., Shaham, Y. K. & Kasevich, M. A. Long-term stability of an area-reversible atom-interferometer Sagnac gyroscope. *Phys. Rev. Lett.* **97**, 240801 (2006).
6. Peters, A., Chung, K. Y. & Chu, S. Measurement of gravitational acceleration by dropping atoms. *Nature* **400**, 849–852 (1999).
7. Weiss, D. S., Young, B. C. & Chu, S. Precision measurement of \hbar/m_C , based on photon recoil using laser-cooled atoms and atomic interferometry. *Appl. Phys. B Lasers Opt.* **59**, 217–256 (1994).
8. Cadoret, M. et al. Combination of Bloch oscillations with a Ramsey-bordé interferometer: New determination of the fine structure constant. *Phys. Rev. Lett.* **101**, <https://doi.org/10.1103/physrevlett.101.230801> (2008).
9. Schlippert, D. et al. Quantum test of the universality of free fall. *Phys. Rev. Lett.* **112**, 203002 (2014).
10. Kasevich, M. & Chu, S. Atomic interferometry using stimulated Raman transitions. *Phys. Rev. Lett.* **67**, 181–184 (1991).
11. Giltner, D. M., McGowan, R. W. & Lee, S. A. Atom interferometer based on Bragg scattering from standing light waves. *Phys. Rev. Lett.* **75**, 2638–2641 (1995).
12. McGuirk, J. M., Snadden, M. J. & Kasevich, M. A. Large area light-pulse atom interferometry. *Phys. Rev. Lett.* **85**, 4498–4501 (2000).
13. Graham, P. W., Hogan, J. M., Kasevich, M. A., Rajendran, S. & Romani, R. W. Mid-band gravitational wave detection with precision atomic sensors. *arXiv:1711.02225* (2017).
14. Canuel, B. et al. Elgar - a european laboratory for gravitation and atom-interferometric research. *arXiv:1911.03701* (2019).
15. Badurina, L. et al. AION: an atom interferometer observatory and network. *J. Cosmol. Astropart. Phys.* **2020**, 011–011 (2020).
16. Dimopoulos, S., Graham, P. W., Hogan, J. M., Kasevich, M. A. & Rajendran, S. Atomic gravitational wave interferometric sensor. *Physical Review D* **78** <https://doi.org/10.1103/physrevd.78.122002> (2008).
17. Chaibi, W. et al. Low frequency gravitational wave detection with ground-based atom interferometer arrays. *Physical Review D* **93** <https://doi.org/10.1103/physrevd.93.021101> (2016).
18. Hild, S. et al. Sensitivity studies for third-generation gravitational wave observatories. *Classical Quantum Gravity* **28**, 094013 (2011).
19. Sathyaprakash, B. et al. Scientific objectives of einstein telescope. *Classical Quantum Gravity* **29**, 124013 (2012).
20. Aasi, J. et al. Advanced LIGO. *Classical Quantum Gravity* **32**, 074001 (2015).
21. Acernese, F. et al. Advanced Virgo: a second-generation interferometric gravitational wave detector. *Classical Quantum Gravity* **32**, 024001 (2014).
22. Arvanitaki, A., Graham, P. W., Hogan, J. M., Rajendran, S. & Tilburg, K. V. Search for light scalar dark matter with atomic gravitational wave detectors. *Physical Review D* **97** <https://doi.org/10.1103/physrevd.97.075020> (2018).
23. El-Neaj, Y. A. et al. AEDGE: Atomic experiment for dark matter and gravity exploration in space. *EPJ Quant Technology* **7** <https://doi.org/10.1140/epjqt/s40507-020-0080-0> (2020).
24. Chiow, S., Kovachy, T., Chien, H.-C. & Kasevich, M. A. 102 $\hbar k$ Large area atom interferometers. *Phys. Rev. Lett.* **107**, 130403 (2011).
25. Müller, H., wey Chiow, S., Long, Q., Herrmann, S. & Chu, S. Atom interferometry with up to 24-photon-momentum-transfer beam splitters. *Phys. Rev. Lett.* **100**, 180405 (2008).
26. Abend, S. et al. Atom-chip fountain gravimeter. *Phys. Rev. Lett.* **117**, 203003 (2016).
27. McDonald, G. D. et al. 80 $\hbar k$ momentum separation with Bloch oscillations in an optically guided atom interferometer. *Phys. Rev. A* **88**, 053620 (2013).
28. Graham, P. W., Hogan, J. M., Kasevich, M. A. & Rajendran, S. New method for gravitational wave detection with atomic sensors. *Phys. Rev. Lett.* **110**, 171102 (2013).
29. Graham, P. W., Hogan, J. M., Kasevich, M. A. & Rajendran, S. Resonant mode for gravitational wave detectors based on atom interferometry. *Phys. Rev. D* **94**, 104022 (2016).
30. Mazzoni, T. et al. Large-momentum-transfer bragg interferometer with strontium atoms. *Phys. Rev. A* **92**, 053619 (2015).
31. Rudolph, J. et al. Large momentum transfer clock atom interferometry on the 689 nm intercombination line of strontium. *Phys. Rev. Lett.* **124**, 083604 (2020).
32. Ushijima, I., Takamoto, M., Das, M., Ohkubo, T. & Katori, H. Cryogenic optical lattice clocks. *Nat. Photonics* **9**, 185–189 (2015).
33. Bloom, B. J. et al. An optical lattice clock with accuracy and stability at the 10⁻¹⁸ level. *Nature* **506**, 71–75 (2014).
34. Muniz, J. A., Young, D. J., Cline, J. R. K. & Thompson, J. K. Cavity-qed determination of the natural linewidth of the ⁸⁷Sr millihertz clock transition with 30 μ Hz resolution. *Phys. Rev. Res.* **3**, 023152 (2020).
35. Trimeche, A., Langlois, M., Merlet, S. & Pereira Dos Santos, F. Active control of laser wavefronts in atom interferometers. *Phys. Rev. Appl.* **7**, 034016 (2017).
36. Ye, J. & Lynn, T. W. Applications of optical cavities in modern atomic, molecular, and optical physics. In *Advances In Atomic, Molecular, and Optical Physics*, 1–83 [https://doi.org/10.1016/s1049-250x\(03\)80003-4](https://doi.org/10.1016/s1049-250x(03)80003-4) (Elsevier, 2003).
37. Hamilton, P. et al. Atom interferometry in an optical cavity. *Phys. Rev. Lett.* **114**, 100405 (2015).
38. Riou, I. et al. A marginally stable optical resonator for enhanced atom interferometry. *J. Phys. B: At., Mol. Optical Phys.* **50**, 155002 (2017).
39. Dovale-Álvarez, M. et al. Fundamental limitations of cavity-assisted atom interferometry. *Phys. Rev. A* **96**, 053820 (2017).
40. Siegman, A. E. *Lasers* (University Science Books, 1986).
41. Nicholson, T. L. et al. Systematic evaluation of an atomic clock at 2×10^{-18} total uncertainty. *Nat. Commun.* **6**, 6896 (2015).
42. Hu, L. et al. Sr atom interferometry with the optical clock transition as a gravimeter and a gravity gradiometer. *Classical Quantum Gravity* **37**, 014001 (2019).
43. Campbell, S. L. et al. A Fermi-degenerate three-dimensional optical lattice clock. *Science* **358**, 90–94 (2017).
44. Yariv, A. *Quantum Electronics* (John Wiley & Sons, Incorporated, 1975).
45. Tomita, I., Sanjoh, H., Yamada, E., Suzuki, H. & Yoshikuni, Y. Theoretical analysis of the generation of multiple wavelengths by pulsed serrodyne modulation. *J. Opt. A: Pure Appl. Opt.* **7**, 701–705 (2005).
46. Ma, S. et al. Efficient high repetition rate electro-optic q-switched laser with an optically active langasite crystal. *Sci. Rep.* **6**, 1–7 (2016).
47. Immarco, A., Steinhacker, M. A., Proebstl, R. J. & Stahl, H. M. Electro-optic q-switch using brewster angle cut pockels cell (1971). US Patent 3,564,450.
48. Black, E. D. An introduction to pound-drever-hall laser frequency stabilization. *Am. J. Phys.* **69**, 79–87 (2001).
49. Goodno, G. D. et al. Investigation of β -BaB₂O₄ as a q switch for high power applications. *Appl. Phys. Lett.* **66**, 1575–1577 (1995).
50. Kim, M. et al. 40 w, 780 nm laser system with compensated dual beam splitters for atom interferometry. *Opt. Lett.* **45**, 6555–6558 (2020).
51. Nourshargh, R., Hedges, S., Langlois, M., Bongs, K. & Holynski, M. Doppler compensated cavity for atom interferometry (2020). 2012.07792.
52. Ludlow, A. D. et al. Systematic study of the ⁸⁷Sr clock transition in an optical lattice. *Phys. Rev. Lett.* **96**, 033003 (2006).
53. Acernese, F. et al. Laser with an in-loop relative frequency stability of 1.0×10^{-21} on a 100-ms time scale for gravitational-wave detection. *Phys. Rev. A* **79**, 053824 (2009).
54. Cummings, E. A., Hicken, M. S. & Bergeson, S. D. Demonstration of a 1-w injection-locked continuous-wave titanium:sapphire laser. *Appl. Opt.* **41**, 7583–7587 (2002).
55. Akerman, N., Navon, N., Kotler, S., Glickman, Y. & Ozeri, R. Universal gate-set for trapped-ion qubits using a narrow linewidth diode laser. *N. J. Phys.* **17**, 113060 (2015).
56. Nadlinger, D. P. Entanglement between trapped strontium ions and photons. (Master's thesis, ETH Zürich, 2016).

Acknowledgements

We thank Y.-H. Lien and J. Goldwin for helpful discussions. This work was supported by the EPSRC under grant number EP/T001046/1 as part of the UK National Quantum Technologies Programme.

Author contributions

R.N. devised the circulating pulse scheme. S.L. derived the theoretical framework and code, and performed the calculations. S.H. and M.L. contributed to the LMT sequence design and Doppler shifts compensation techniques. K.B. and M.H. contributed throughout and supervised the research. All authors contributed to reviewing and assessing the results, and to the development and review of the manuscript.

Competing interests

The authors declare no competing interests.

Additional information

Correspondence and requests for materials should be addressed to Michael Holynski.

Peer review information *Communications Physics* thanks the anonymous reviewers for their contribution to the peer review of this work.

Reprints and permission information is available at <http://www.nature.com/reprints>

Publisher's note Springer Nature remains neutral with regard to jurisdictional claims in published maps and institutional affiliations.



Open Access This article is licensed under a Creative Commons Attribution 4.0 International License, which permits use, sharing, adaptation, distribution and reproduction in any medium or format, as long as you give appropriate credit to the original author(s) and the source, provide a link to the Creative Commons license, and indicate if changes were made. The images or other third party material in this article are included in the article's Creative Commons license, unless indicated otherwise in a credit line to the material. If material is not included in the article's Creative Commons license and your intended use is not permitted by statutory regulation or exceeds the permitted use, you will need to obtain permission directly from the copyright holder. To view a copy of this license, visit <http://creativecommons.org/licenses/by/4.0/>.

© The Author(s) 2021